Circumventing Radical Generation on Fe-V Atomic Pair Catalyst for Robust Oxygen Reduction and Zinc-Air Batteries

Lan Ran†[a], Yichen Zhang†[b], Wenming Tong[c], Long Chen[a], Maoyu Wang[e,f], Hua Zhou[f], Pau Farràs*[c], Shanyong Chen*[a,d], Xiaoqing Qiu*[a]

a. L. Ran, L. Chen, Dr. S. Chen, Prof. X. Qiu
College of Chemistry and Chemical Engineering
Central South University
410083, Changsha, China
E-mail: shanyongchen@csu.edu.cn, xq-qiu@csu.edu.cn

b. Y. Zhang
Institute of Applied Chemistry, Department of Chemical Engineering
Tsinghua University
100084, Beijing, China

c. Dr. W. Tong, Dr. P. Farràs
School of Biological and Chemical Sciences, Ryan Institute
University of Galway
H91 TK33, Galway, Ireland
E-mail: pau.farras@universityofgalway.ie.

d. Dr. S. Chen
Guangdong Key Laboratory of Environmental Pollution and Health, School of Environment
Jinan University
511443, Guangzhou, China

e. Dr. M. Wang
Shanghai Synchrotron Radiation Facility, Shanghai Advanced Research Institute
Chinese Academy of Sciences
201204, Shanghai, China.

f. Dr. M. Wang, Prof. H. Zhou
X-ray Science Division
Argonne National Laboratory
60439, Lemont, IL, United States

Abstract: Iron-nitrogen-carbon (Fe-N-C) catalysts are considered the most active platinum-free alternative for oxygen reduction reaction (ORR), yet the generated reactive oxygen species (ROS) from general mechanistic pathway rapidly impair the ORR activity and stability of Fe-N-C. Herein, we establish and report an ORR pathway-switching strategy to circumvent ROS generation and fundamentally improve the activity and stability of Fe-N-C via DFT guided catalyst design. The constructed Fe-V atomic pair catalyst (Fe_1V_1-NC) with N_2Fe-N_2-VN_2 configuration enables side-on adsorption of O_2 and subsequent direct-breaking of the O=O bond to form O*, thereby avoiding the formation of ROS radicals. Importantly, there is inter-site electron interactions between FeN_4 and VN_4, which further boost the ORR activity. Consequently, Fe_1V_1-NC exhibits outstanding ORR activity with onset and half-wave ($E_{1/2}$) potentials at 1.02 and 0.89 V vs. RHE, respectively, in 0.1 M KOH. Record-high stability is achieved on Fe_1V_1-NC with a minimal decay in $E_{1/2}$ by 16 mV over 50,000 cycles, surpassing Fe-N-C counterpart and most of the catalysts reported to date. The Fe_1V_1-NC-based zinc-air battery reported here demonstrates exceptional durability up to 400 h at 10 mA·cm^{-2}. This work identifies the intrinsic correlation between ORR pathway, activity, and stability, advancing development of stable catalytic systems.

Introduction

Developing cost-effective oxygen reduction reaction (ORR) electrocatalysts is crucial for the next-generation energy conversion and storage devices, such as metal-air batteries and fuel cells, that are environmentally friendly[1-3]. Currently, platinum-group-metal-based (PGM) catalysts have been recognized as having optimal electrocatalytic activity for cathodic ORR reaction. However, their scarcity and economic viability seriously limit the large-scale applications [4-7]. Great efforts have been devoted to exploiting efficient PGM-free alternatives [8-10]. Wherein, transition metal-nitrogen-carbon (M-N-C) catalysts exhibit prominent initial ORR activity, among which Fe-N-C has been widely reported as one of the most promising alternatives to PGM catalysts[11-14]. However, Fe-N-C catalysts are widely proven to show unsatisfactory durability, typically experiencing 50-70% degradation over tens of hours during a long-term ORR operation[15-18]. Notably, the reactive oxygen species (ROS), including ·OH and ·OOH generated during an ORR process, are regarded as one of the most probable causes of degradation for Fe-N-C[19-21]. The ROS species could ferociously attack carbon carriers to promote demetallation or even direct destruction of the Fe-N_x active sites in Fe-N-C, leading to a sharp decline in its ORR activity and stability[22-24]. This has, therefore, become one of the great challenges in further developing practical applications for the utilization of Fe-N-C.

Previous efforts to improve the durability of Fe-N-C have mainly focused on introducing scavengers[25-26], which could trap the generated ROS radicals and, thus, mitigate degradations in the ORR activity[27-28]. PtFe alloys, when implanted into the Fe-N-C matrix, have been shown to effectively lower H_2O_2 production and harmful oxygen-containing radicals[29]. Ta-TiO_x nanoparticle as additives to Fe-N-C has led to the suppression of H_2O_2 yield by 51% at 0.7 V and an enhancement in the stability of the corresponding fuel cell with a current density decay of only 3% at 0.9 $V_{iR\text{-}free}$, demonstrating an excellent ROS scavenging ability.[30] Our recent study[31] also reported Mn single atom tuning Fe-N-C catalysts, where the generated ROS can be scavenged on Mn sites. Clearly, the introduction of radical scavenging sites appears to improve ORR stability of Fe-N-C to a certain degree. Nevertheless, the ROS radicals, once generated, will inevitably poison neighboring Fe active sites as

illustrated in Figure 1a[32-34]. That is to say, radical scavengers play a limited role in improving the intrinsic ORR stability. Moreover, some of the inactive oxides employed as radical scavengers may even reduce the mass-specific activity of Fe-N-C[29, 35]. Undoubtedly, more fundamental and effective strategies are needed to circumvent ROS generation during ORR to improve the intrinsic activity and stability. Mechanistically, an ORR process typically follows an associative pathway that includes formation of OOH* intermediates[36-37] with generations of many ROS radicals. In contrast, direct cleavage of O=O bond via the dissociative pathway could potentially circumvent the step where the formation of ROS occurs [12, 38]. Such direct engineering of ORR mechanistic pathway for Fe-N-C would lead to an avoidance of ROS generation at the source level and, thereby, fundamentally improving ORR activity and stability. To the best of our knowledge, few studies have noticed the effect of ORR pathway on operational stability, which is theoretically valid but remains unexplored.

In this work, we propose an ORR pathway-switching strategy via constructing Fe-V atomic pairs in Fe-N-C matrix to enhance its intrinsic stability. As depicted in Figure 1b, the adsorption of O_2 on the Fe-V atomic pair with a side-on orientation would result in a direct cleavage of O=O bonding to form O* and, hereby, preventing the formation of H_2O_2 and OOH* intermediates. Unlike the general strategy that relies on external scavengers to trap ROS radicals generated from H_2O_2 and OOH* intermediate, the proposed unique ORR pathway on Fe-V atomic pairs enables avoiding the step that proceed to generate ROS radicals. We first construct three theoretical models, which are then evaluated by DFT calculations under various scenarios according to the respective mechanistic ORR pathways. We then experimentally validate the proposed ORR pathway-switching strategy. The synthesized catalysts, such as Fe_1V_1-NC and Fe_1-NC, are investigated by a series of advanced characterization techniques and thoroughly assessed electrochemically for catalytic properties toward ORR. We employ a range of in situ and ex situ techniques to confirm that the improved ORR activity and stability are due to the successful suppression of ROS radical generation. We ultimately show the ORR activity and stability of Fe_1V_1-NC at the device level by applying it to a zinc-air battery as the cathode catalyst.

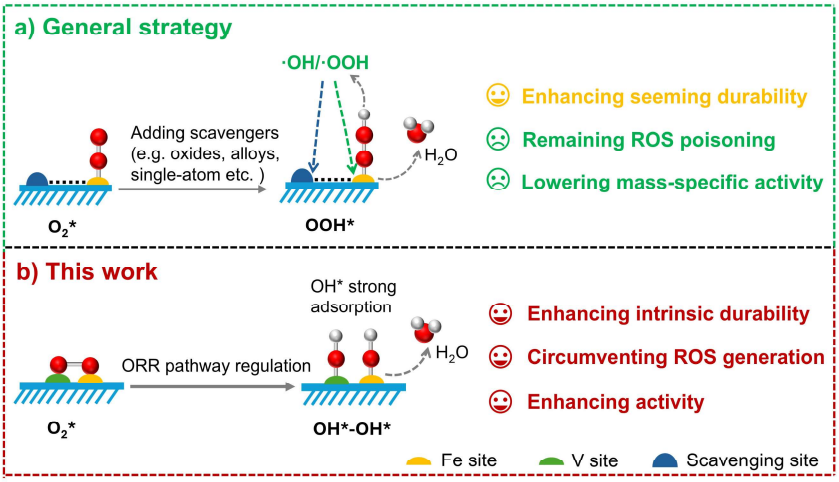

Figure 1. Illustration of the strategies to improve the ORR activity and stability of Fe-N-C in (a) previous reports and (b) this study.

Results and Discussion

Theoretical analysis on ORR pathway effect

Density functional theory (DFT) calculations were initially employed to evaluate the impact of 4e- ORR pathways (associative and dissociative) on catalytic behavior[39]. As shown in Figures S1 and S2, these theoretical models were constructed with consideration of axial OH* adsorption, which is attributed to the spontaneous adsorption behavior as reported in previous studies [39]. For the Fe_1V_1-NC model with OH* adsorption, the dissolution potentials of Fe and V are calculated to be 0.920 V and 0.597 V, respectively. Conventional Fe_1-NC catalyst (Figure S3) follows the associative ORR pathway, where O_2 is adsorbed in an end-on configuration at the Fe sites, undergoes protonation prior to O=O bond cleavage, and proceeds to subsequent conversion. The specific reaction pathway is: $O_2 \rightarrow O_2^* \rightarrow OOH^* \rightarrow O^* \rightarrow OH^* \rightarrow H_2O$ (Figure 2a), during which the generated OOH* intermediates tend to desorb to become ·OOH radicals, which can further transform into ·OH radicals. These ·OOH and ·OH radicals, as oxidative species, readily cause severe corrosion to Fe sites and carbon substrate, leading to active site damage and reduced stability of Fe_1-NC. In contrast, the Fe_1V_1-NC with dual-metal sites shown in Figure 2b follow the dissociative ORR pathway, where O_2 is adsorbed via a side-on bridging configuration between Fe and V sites, and the O=O bond cleaves directly before the subsequent protonation. The specific reaction pathway is: $O_2 \rightarrow O_2^* \rightarrow O^*\text{-}O^* \rightarrow OH^*\text{-}O^* \rightarrow OH^*\text{-}OH^* \rightarrow OH^* \rightarrow H_2O$. This process circumvents the formation of OOH* intermediates, thereby preventing the generation of ·OOH radicals and further transformation. The different reaction pathways in ORR may lead to distinct reaction kinetics and activity. Through analyzing reaction potentials between the two pathways (Table S1), the dissociative pathway on Fe_1V_1-NC necessitates a smaller overpotential (i.e. a higher onset potential) compared to associative pathway, evidencing a

preference for dissociative pathway. In addition, the free energy diagrams at both equilibrium and onset conditions confirm the favorability of dissociative pathway on Fe_1V_1-NC catalyst over associative pathway (Figures S4-5). We also computed the free energy diagram and onset potential for H_2O_2 formation (2e- ORR) on Fe_1V_1-NC (Figure S6). Result shows much lower onset potential of 2e- ORR relative to 4e- ORR (Table S1), indicating the dominated 4e- ORR over 2e- ORR. Additionally, the free energy diagrams of oxygen evolution reaction (OER) for Fe_1V_1-NC and Fe_1-NC (Figure S7) show that the OER overpotential for Fe_1V_1-NC and Fe_1-NC is 0.660 and 0.788 V vs. RHE, respectively.

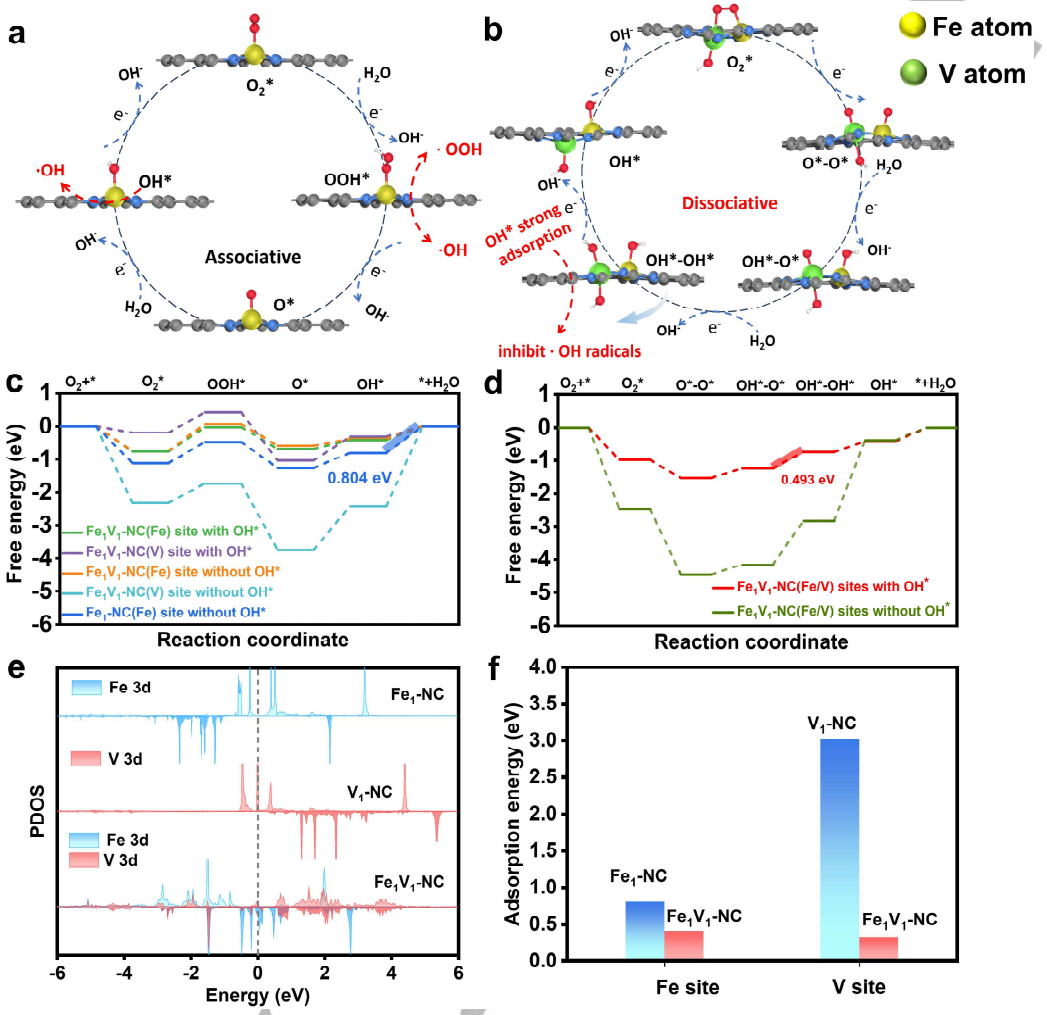

Figure 2. Schematic diagram of (a) associative pathway for Fe_1-NC and (b) dissociative pathway for Fe_1V_1-NC. Free energy diagram of ORR on (c) Fe or V single site and (d) Fe-V dual sites. (e) The PDOS of central metal atoms in Fe_1-NC, V_1-NC and Fe_1V_1-NC. (f) Adsorption energy of OH* on the metal sites of Fe_1-NC, V_1-NC and Fe_1V_1-NC.

We further investigated the detailed processes of ORR pathway on different models, with the corresponding free energy diagrams shown in Figures 2c-2d. The V sites show thermodynamically favorable strong adsorption of O_2 (ΔG_{O2^*} = -2.31 eV) but high barrier for OH* desorption (ΔG_{OH^*} = 1.19 eV). Therefore, the OH* will be retained on the V site to form axial adsorption. Interestingly, the axial OH* adsorption configuration on V sites (*OH-V-N_4) induces a greatly reduced ΔG for the potential-determining step (PDS) compared to pristine V-N_4 sites, while the axial OH* adsorption configuration on Fe sites generates finite effects. The PDS on Fe_1-NC is the transformation of OH* into H_2O, with a ΔG value of 0.804 eV. The PDS for Fe_1V_1-NC is the step of OH*-O* to OH*-OH*, which exhibits a lower ΔG value of 0.493 eV. The reduced ΔG for Fe_1V_1-NC indicates an enhanced ORR activity. Additionally, we calculated the projected density of states (PDOS) for the d-orbitals of Fe_1-NC, V_1-NC, and Fe_1V_1-NC respectively (Figure 2e). Fe_1V_1-NC exhibits a broader PDOS near Fermi level than that of Fe_1-NC and V_1-NC, suggesting enhanced charge transfer capability [41]. Moreover, the d-band centers of Fe (-0.754 eV) and V (0.240 eV) in Fe_1V_1-NC are significantly lower than those in Fe_1-NC (-0.428 eV) and V_1-NC (1.425 eV), suggesting presence of electron interaction between Fe and V. Such an interaction creates an electron-rich Fe-V interface that facilitates O_2 activation and more efficient charge transfer, promoting ORR process. The adsorption energies of OH* radical on the metal sites of Fe_1-NC, V_1-NC, and Fe_1V_1-NC were further investigated to evaluate their ·OH formation process. Figure 2f shows the adsorption energies of OH* on the Fe and V sites in Fe_1V_1-NC are stronger than those on Fe_1-NC and V_1-NC. This indicates that OH* intermediates are more stably adsorbed on Fe_1V_1-NC, which facilitates the subsequent ORR process rather than the intermediates desorbing to form ·OH as occurs with Fe_1-NC. In 2e- ORR pathway on Fe_1V_1-NC, the strong adsorption of OOH* on Fe and V sites (Figure S6) hinder its desorption and subsequent formation of •OOH radical. In summary, the catalyst with Fe_1-V_1 atomic pair presents unique ORR features. Fe_1V_1-NC catalyzes the dissociative ORR pathway to enhance intrinsic

ORR stability by avoiding the formation of ROS radicals, and generates a site-electron interaction that boosts ORR activity.

Synthesis and Characterization

The Fe-V atomic pair in Fe_1V_1-NC catalyst was synthesized via the approach shown in Figure 3a. Fe and V were anchored onto zeolitic imidazole framework (ZIF-8), and the resulting Fe,V-ZIF-8 were subsequently pyrolyzed under N_2 atmosphere at 910 °C. During the pyrolysis, Fe and V atoms are coordinated with N atoms to form atomically dispersed active sites in the carbon skeleton while Zn is evaporated substantially owing to its relatively lower boiling point[42]. The Fe_1-NC and V_1-NC were synthesized by using the same method without respective V and Fe salts in the precursors. Note that Fe_1V_1-NC-1:3 and Fe_1V_1-NC-3:1 indicate the corresponding molar ratio of Fe to V salts is 1:3 or 3:1 during the preparation process respectively.

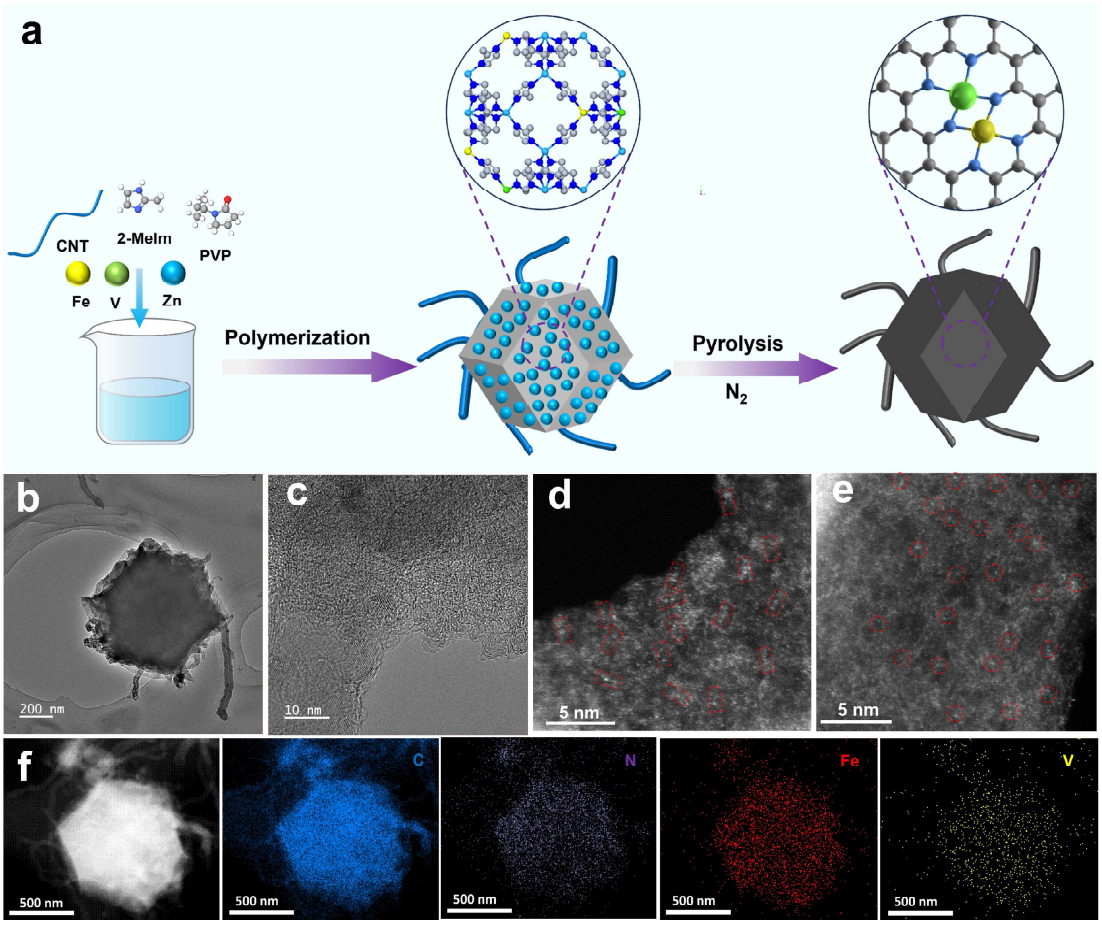

Figure 3. (a) Schematic illustration of the synthesis of Fe_1V_1-NC. (b) TEM image and (c) HR-TEM image of Fe_1V_1-NC. AC-HAADF-STEM images of (d) Fe_1V_1-NC (The red squares represent Fe-V diatomic pairs) and (e) Fe_1-NC (The red circles represent Fe single atoms.). (f) Elemental mapping for Fe_1V_1-NC.

Scanning electron microscopy (SEM) and transmission electron microscopy (TEM) are employed to analyze the morphology of the catalysts. Fe_1-NC, V_1-NC, and Fe_1V_1-NC consist of uniform polyhedral structure with carbon nanotubes anchored to its surface, which is inherited from ZIF-8. However, Fe_1V_1-NC-1:3 and Fe_1V_1-NC-3:1 with unmatched metal ratios demonstrate nanotubes as the major morphology with much fewer polyhedral structures (Figure 3b-c and S8). The TEM and corresponding energy dispersive spectroscopy (EDS) element mapping indicate even dispersions of metal elements in the carbon skeleton without obvious clusters or metal particles (Figure 3f and Figures S9-10). The aberration-corrected high-angle annular dark-field scanning transmission electron microscopic (AC-HAADF-STEM) measurements reveal that metal elements are dispersed at atomic levels as featured by the highlighted bright spots appearing in pairs for Fe_1V_1-NC in Figure 3d. Additionally, atomically dispersed Fe atoms are observed on Fe_1-NC, with isolated bright spots (Figure 3e). An inductively coupled plasma optical emission spectrometry (ICP-OES) analysis determines the content of Fe and V in Fe_1V_1-NC to be 0.84 wt.% and 0.73 wt.% respectively, which is a near the 1 : 1 atomic ratio (1.04 : 1) for Fe : V as summarized in Table S2.

Powder X-ray diffraction (XRD) patterns of Fe_1V_1-NC, Fe_1-NC, V_1-NC, Fe_1V_1-NC-1:3, and Fe_1V_1-NC-3:1 are shown in Figure S11. All the catalysts show diffraction peaks at 26.2° and 43.2° belonging to the (002) and (101) crystal planes of graphitic carbon, respectively[43]. No diffraction peaks associated with metallic Fe or V species were detected in Fe_1-NC, V_1-NC and Fe_1V_1-NC, corroborating the highly dispersed nature of Fe and V species in the carbon substrate. However, additional diffraction peaks of metal and/or their oxide nanoparticles were apparent for Fe_1V_1-NC-1:3 and Fe_1V_1-NC-3:1, indicating that precise control of the metal content is crucial for the synthesis of atomically dispersed catalysts. Furthermore, the defects and graphitization of the catalysts were analyzed by Raman spectroscopy (Figure S12). Two prominent peaks are observed at 1333 and 1569 cm^{-1}, corresponding to D and G bands, respectively. The peak intensity ratios of G and D bands (I_G/I_D)

for Fe_1-NC, V_1-NC, and Fe_1V_1-NC are calculated to be 1.32, 1.53, and 1.42, respectively, implying that the introduction of V species improves the degree of graphitization. Such prominence of G band relative to D band in all the catalysts due to the high graphitization degree is advantageous for electrochemical conductivity. The specific surface area and structural porosity were characterized by Brunauer-Emmett-Teller (BET) N_2 adsorption-desorption isotherms. As shown in Figure S13, the three catalysts demonstrate type-IV isotherm with abundant micropores and mesopores. Fe_1V_1-NC features a large surface area of 648.0 $m^2 \cdot g^{-1}$ compared to Fe_1-NC (365.5 $m^2 \cdot g^{-1}$) and V_1-NC (438.8 $m^2 \cdot g^{-1}$), suggesting exposure of more active sites with Fe_1V_1-NC. The total pore volume of Fe_1V_1-NC is measured to be 0.351 $cm^3 \cdot g^{-1}$ with an average 2.169 nm pore size (Table S3). The abundant micropores and mesopores are beneficial to increasing accessibility of active sites and enhancing mass transfer kinetics.[44] These characteristics highlight a promising potential of Fe_1V_1-NC for catalyzing ORR process. O_2 temperature-programmed desorption (O_2-TPD) measurements indicate that the V_1-NC exhibits a stronger adsorption capability for O_2 and O_2-containing intermediates compared to Fe_1-NC as evidenced by the higher O_2 desorption temperature in Figure S14, demonstrating the importance of V sites in Fe_1V_1-NC for ORR. [45]

The chemical composition and electron interaction of the catalysts were investigated by X-ray photoelectron spectroscopy (XPS). The XPS survey spectrum confirms the presence of C, N, O, Fe, and V in Fe_1V_1-NC (Figure S15). The atomic contents of Fe and V in Fe_1V_1-NC obtained from XPS analysis are 1.72% and 1.64% (close to 1:1), respectively, as summarized in Table S4, and consistent with the result obtained by ICP-OES in Table S2. The high-resolution C 1s spectrum (Figure S16) was deconvoluted into three peaks, which are assigned to C-C (284.8 eV), C-N (285.4 eV), and C=O (286.9 eV). The C-N bond indicates the successful incorporation of N into carbon matrix, which provides anchoring sites for metal atoms[46-47]. The high-resolution N 1s spectra of Fe_1-NC, V_1-NC, and Fe_1V_1-NC are deconvoluted into four peaks respectively, including pyridinic N (398.4 eV), metal-N (398.9 eV), pyrrolic N (399.7 eV), and graphitic N (401.2 eV) (Figure S17a). The distinct metal-N peak implies the formation of coordination between N and Fe/V. Importantly, the higher contents of metal-N and graphitic N are induced by incorporating V element for Fe_1V_1-NC with respect to Fe_1-NC and V_1-NC (Figure S17b and Table S5), in good agreement with Raman results. The rich graphitic N is beneficial for improving limiting diffusion current density and corrosion resistance of the carbon substrate. The high-resolution Fe 2p spectrum of Fe_1V_1-NC in Figure 4a can be fitted to the sum of five peaks. The peaks at 709.5 (Fe $2p_{3/2}$) and 723.2 eV (Fe $2p_{1/2}$) correspond to Fe^{2+} species, while the peaks located at 712.5 (Fe $2p_{3/2}$) and 726.2 (Fe $2p_{1/2}$), belong to Fe^{3+} species. The peak at 717.0 eV is the satellite peak. Such an analysis indicates that Fe mainly coordinates with N to form $Fe^{2+/3+}$-N_x moieties. Notably, compared with Fe_1-NC, the Fe 2p peaks of Fe_1V_1-NC exhibit a slight shift by 0.5 eV toward the lower binding energy, suggesting an electron enrichment effect at Fe sites. These results suggest the existence of a strong inter-site electron interaction between Fe and V sites, which can modulate the reaction electron state for excellent ORR activity.[48]

X-ray absorption spectroscopy (XAS) was used to further elucidate the coordination environment and electronic structure of Fe and V sites in the catalysts. As shown in X-ray absorption near-edge spectroscopy (XANES) (Figure 4b), the Fe K-edge absorption edges of both Fe_1V_1-NC and Fe_1-NC are located at higher energy position relative to Fe foil, proving an oxidized state of the metal centers. Importantly, the Fe K-edge of Fe_1V_1-NC exhibits a slightly lower adsorption edge than that of Fe_1-NC, implying a comparatively electron-enriched state of Fe site for Fe_1V_1-NC. Similarly, the V K-edge XANES spectrum of Fe_1V_1-NC exhibits a positive energy shift relative to V foil (Figure S18). The XAS analysis agrees well with XPS results, jointly confirming the site-to-site electron interaction for Fe_1V_1-NC. In addition, the Fourier transforms (FT) of the K-edge extended X-ray absorption fine structures (EXAFS) for Fe_1V_1-NC and Fe_1-NC show a dominant peak at ~1.4 Å, corresponding to Fe-N scattering path (Figure 4c). Fe-Fe coordination is absent in both Fe_1V_1-NC and Fe_1-NC, confirming the atomically dispersed nature of Fe. Similarly, the dominant peak at ~1.3 Å in the V-edge EXAFS spectrum is assigned to V-N scattering path with the absence of V-V bond in Fe_1V_1-NC. Furthermore, the quantitative least-squares fitting of EXAFS was performed (Figure 4d), with the corresponding fitting results summarized in Table S6. The coordination numbers (CN) of Fe-N and V-N in Fe_1V_1-NC are determined to be 3.90 and 3.83 respectively. This finding confirms that Fe and V are coordinated with four N atoms, forming a N_2Fe-N_2-VN_2 configuration in Fe_1V_1-NC, where Fe and V are bridged by N atoms with no direct bonding between Fe and V. This is consistent with AC-HADDF-STEM analysis that Fe single atom is adjacent to V atom site within the Fe-V atomic pair. Additionally, Fe_1-NC fits well with typical Fe-N_4 model, in which the Fe is coordinated with four pyridinic N atoms (Figure S19). Both Fe and V foils fit well with obvious Fe-Fe and V-V configuration (Figure S20). The wavelet transform (WT) for EXAFS oscillations of Fe_1V_1-NC and Fe_1-NC is performed to provide high-resolution visualization of the metal atomic sites with both radial distance and k-space (Figure 4e). Notably, the WT signals of Fe-Fe (~9.0 $Å^{-1}$) and V-V (~9.1 $Å^{-1}$) for Fe foil and V foil, respectively, are clearly observed. The WT contour plots of Fe_1-NC and Fe_1V_1-NC exhibit maximum intensities at ~5.2 $Å^{-1}$, corresponding to the Fe-N scattering path. Meanwhile, the maximum intensity of WT contour appears at ~2.4 $Å^{-1}$ for Fe_1V_1-NC, which is attributed to the V-N scattering path. Compared to Fe foil and V foil, the Fe-Fe or V-V signals are absent in Fe_1-NC, V_1-NC, and Fe_1V_1-NC, confirming the absence of metal nanoparticles. These findings demonstrate that Fe and V atoms exist in atomically dispersed form in Fe_1V_1-NC and feature N_2Fe-N_2-VN_2 configurations.

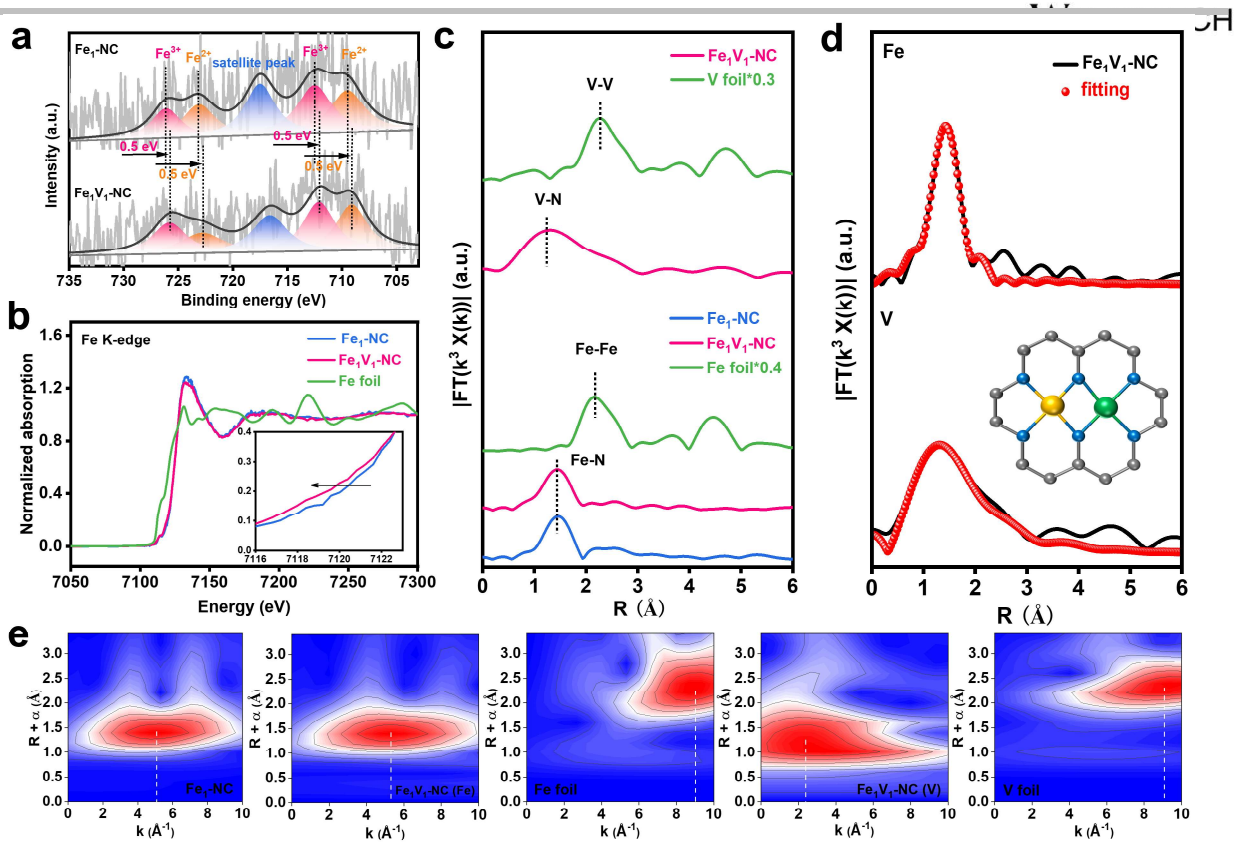

Figure 4. (a) Fe 2p XPS spectra for Fe_1-NC and Fe_1V_1-NC. (b) Fe K-edge XANES spectra (the inset shows a partial enlargement of the area near the onset of the near edge). (c) Fourier transform of k^3-weighted EXAFS spectra of Fe_1V_1-NC, Fe_1-NC, and reference Fe and V foils. (d) FT-EXAFS fitting curves of Fe_1V_1-NC in R space (the inset is optimized configuration of Fe_1V_1-NC). (e) Wavelet transforms of k^3-weighted EXAFS spectra of Fe_1-NC, Fe_1V_1-NC (Fe), Fe foil, Fe_1V_1-NC (V), and V foil.

Electrocatalytic ORR performance

The ORR performances of the catalysts were evaluated via cyclic voltametric (CV) and linear sweep voltametric (LSV) measurements in 0.1 M KOH electrolyte using a three-electrode system equipped with a rotating ring disk electrode (RRDE). The CV curves of all prepared catalysts (Fe_1V_1-NC, Fe_1-NC, V_1-NC, Fe_1V_1-NC-1:3, and Fe_1V_1-NC-3:1) and commercial Pt/C exhibit rather significant reduction peaks (prominent ORR responses) in an O_2 saturated electrolyte than an Ar-saturated environment (Figure 5a and S21), with Fe_1V_1-NC exhibiting the most positive reduction peak position and, therefore, the best ORR activity. Figures 5b and S22 present LSV curves of all the catalysts and commercial Pt/C with a scan rate at 10 mV·s^{-1} with a rotation speed at 1600 rpm. As expected, Fe_1V_1-NC demonstrates superior ORR activity in terms of both onset potential (E_{onset}) and half-wave potential ($E_{1/2}$), reaching an ultrahigh E_{onset} at 1.02 V and $E_{1/2}$ at 0.89 V. In comparison, the values for other catalysts are as following: Fe_1-NC (E_{onset} = 0.98 V, $E_{1/2}$ = 0.85 V), V_1-NC (E_{onset} = 0.94 V, $E_{1/2}$ = 0.75 V), and commercial Pt/C (E_{onset} = 0.99 V, $E_{1/2}$ = 0.85 V), respectively. The ORR kinetics is verified by the Tafel plot in Figure 5c and S23. The lower Tafel slope of Fe_1V_1-NC (103.8 mV·dec^{-1}) indicates its enhanced reaction kinetics than that of commercial Pt/C (111.7 mV·dec^{-1}). Moreover, the kinetic current density (J_k) at 0.85 V for Fe_1V_1-NC (50.1 mA·cm^{-2}) is also 2.5, 5.8 and 1.8 times higher than that of Fe_1-NC (20.2 mA·cm^{-2}), V_1-NC (8.6 mA·cm^{-2}), and commercial Pt/C (28.6 mA·cm^{-2}) (Figure 5d), suggesting a fast ORR reaction. The electrochemical double-layer capacitance from CV curves is calculated to evaluate the electrochemically active surface area (ECSA). Shown in Figure S24, the ECSA of Fe_1V_1-NC is comparable to that of Fe_1-NC and V_1-NC, which excludes the interference of site density when comparing ORR activities. Fe_1V_1-NC is also found to exhibit better OER activity than Fe_1-NC with lower onset potentials (Figure S25). The electron transfer number (*n*) is determined based on rotating disk electrode (RDE) measurements at different rotating speeds varying from 400 to 2500 rpm. The corresponding Koutecky-Levich (K-L) curves (Figures S26-30) show that the calculated *n* values for Fe_1V_1-NC in the potentials ranging from 0.2 to 0.6 V are between 3.93 to 3.97, which are very close to the standard 4e$^-$ transfer process. The electron transfer number and H_2O_2 yield are further investigated using a RRDE. Figure S31 confirms once again the high-efficiency 4e$^-$ ORR process catalyzed by Fe_1V_1-NC with an approximate electron transfer number of 3.98. Importantly, the H_2O_2 yield by Fe_1V_1-NC is maintained below 4.7% throughout the potentials range of 0.1-0.8 V vs. RHE, which is much more consistent and lower than that of Fe_1-NC (9.8%) and V_1-NC (14.9%) (Figure 5e). This reveals that the dissociative path followed by Fe_1V_1-NC efficiently inhibits H_2O_2 generation and promotes 4e$^-$ ORR, as well as mitigates the attack by the corrosive peroxide and hydroxyl radials (•OOH/•OH) all the while maintaining the superior ORR activity.

The electrochemical impedance spectra (EIS) in Figure S32 demonstrate the similar shape of semicircles for all the catalysts. The EIS for Fe_1V_1-NC exhibits the smallest diameter, which unveils the lowest charge-transfer resistance and the enhanced ORR reaction kinetics. The anti-methanol ability was evaluated by measuring chronoamperometric responses (i-t) of ORRs by Fe_1V_1-NC and Pt/C to an injection of 3 mL methanol into the electrolyte at 500 s as shown in Figure S33. Fe_1V_1-NC exhibits a stable relative current with little to no disturbance upon the injection, whereas the commercial Pt/C demonstrates a sharp decline in the relative current upon the injection with a gradual and partial current recovery afterward under the same condition. We probed the OH* adsorption on V sites in V_1-NC using KSCN poisoning experiment. Generally, the KSCN has distinct poisoning effect on V sites in V_1-NC (Figure S34). However, once V_1-NC has gone through ORR, the poison effect of KSCN is negligible. These findings imply that V sites tend to generate spontaneously axial OH* adsorption during ORR, which prevents them from being seriously poisoned. This provides experimental support for presence of OH* adsorption on V_1-NC, consistent with previous theoretical analysis.

With the excellent ORR performance achieved above, we now evaluate the electrocatalytic ORR stability. Firstly, the long-term stabilities of Fe_1V_1-NC, Fe_1-NC, and commercial Pt/C were evaluated by measuring chronoamperometry (I-t) at 0.5 V vs. RHE (Figure 5f). Fe_1V_1-NC demonstrates superior stability with the relative current being maintained over 95% throughout the continuous ORR process for 24 h. In sharp contrast, Fe_1-NC displays a rapid attenuation of the current density to ~60%. The commercial Pt/C shows a better stability than Fe_1-NC but far inferior than Fe_1V_1-NC. In addition, we performed accelerated durability tests (ADT) to further probe the stability of the catalysts (Figure 5g-h). Fe_1V_1-NC observes a loss in the $E_{1/2}$ by only 16 mV after 50,000 CVs, showcasing its remarkable stability. For Fe_1-NC, a test of 15,000 CVs already leads to a loss in $E_{1/2}$ by 31 mV. The stability of Fe_1V_1-NC in this work is also at the record-high level when compared to the catalysts reported previously (Figure 5i and Table S7), with the loss in $E_{1/2}$ as low as 3.2×10^{-4} mV per CV cycle for 50,000 cycles.

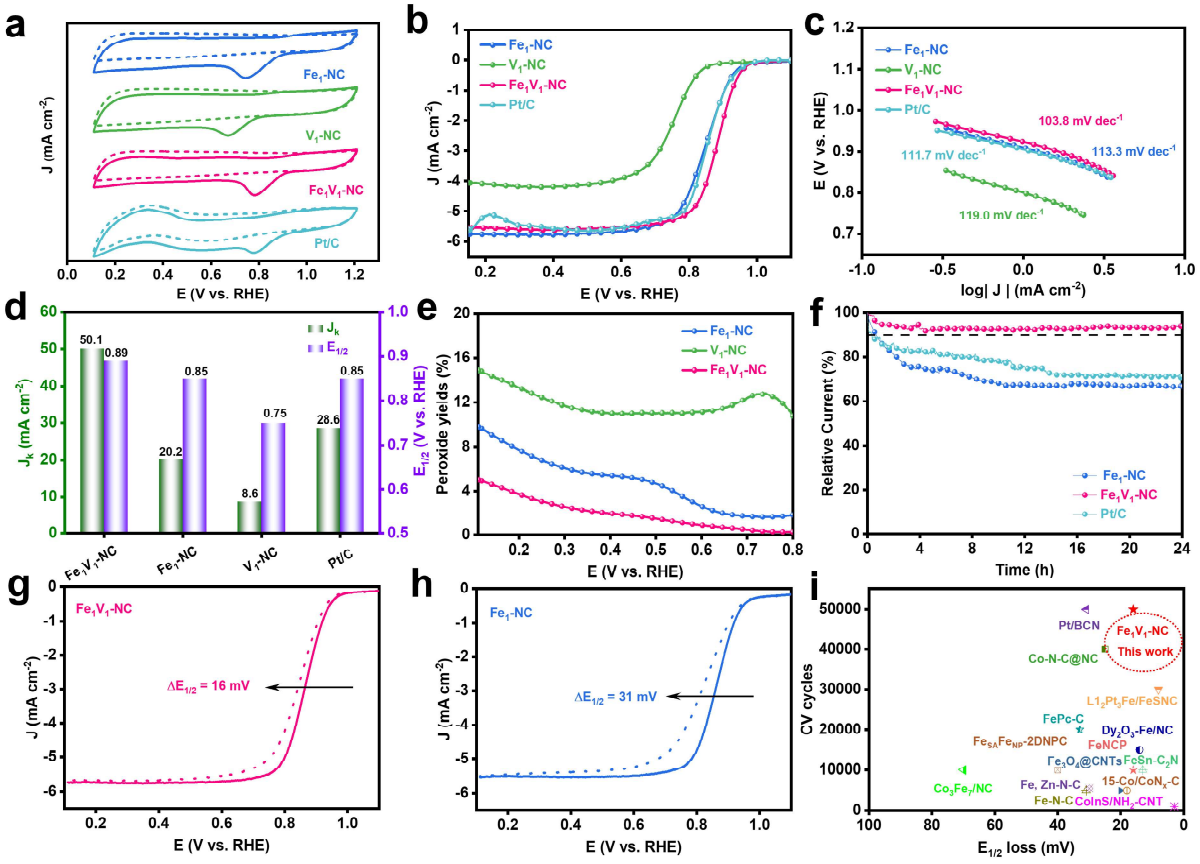

Figure 5. (a) CV curves in O_2-saturated (solid line) and Ar-saturated (dashed line) electrolyte solutions respectively. The scan rate is 50 mV·s^{-1}. (b) LSV polarization curves in O_2-saturated 0.1 M KOH solution. (c) Transferred Tafel slope from the LSV curves. (d) Comparison of the J_k at 0.85 V and $E_{1/2}$. (e) H_2O_2 yield and (f) I-t curves of Fe_1-NC, Fe_1V_1-NC and Pt/C. LSV curves of (g) Fe_1V_1-NC and (h) Fe_1-NC before and after ADT tests. (i) $E_{1/2}$ decays compared with those reported in the literature. These data are also summarized in Table S7 with references.

Investigation of ROS radical generation

As reported previously[49], the generation of corrosive ROS during ORR causes serious damage for carbon-supported Fe-N_x sites, which is the major reason for the deactivation of Fe-N-C catalysts. This is corroborated by our preliminary exploration of the effect of ROS on the ORR performance of Fe_1-NC, where we observe a significant decline in $E_{1/2}$ under a ROS-rich condition (Figure S35). To investigate the mechanism of stability enhancement, we focus on the ORR pathway and its effect on ROS generation process for Fe_1-NC and Fe_1V_1-NC. The key reaction intermediates of Fe_1-NC and Fe_1V_1-NC during ORR process were monitored *in situ* using attenuated total reflection surface-enhanced infrared absorption spectroscopy (ATR-SEIRAS). Figure 6a shows the spectra for the Fe_1-NC catalyzed ORR, in which the characteristic absorption peaks all three

intermediate species (OOH* at ~1027 cm^{-1}, OH* at ~1200 cm^{-1}, and *O at ~950 cm^{-1}) are present[50]. However, only signals attributed to OH* (~1116 cm^{-1}) and *O (964 cm^{-1}) are observed for the Fe_1V_1-NC catalyzed ORR (Figure 6b). These results confirm that Fe_1V_1-NC follows a dissociation pathway without the formation of OOH* intermediate, thereby preventing formation of ·OOH, H_2O_2, and associated ROS radicals. Furthermore, the OH* signal for Fe_1V_1-NC is more distinct than for Fe_1-NC, which implies a stronger adsorption of OH* onto Fe_1V_1-NC. The strong adsorption facilitates rapid intermediate conversion while suppressing desorption-induced formation of ·OH radical. The ability of Fe_1V_1-NC to circumvent ROS radical generation is consistent with the DFT analysis in Figure 2.

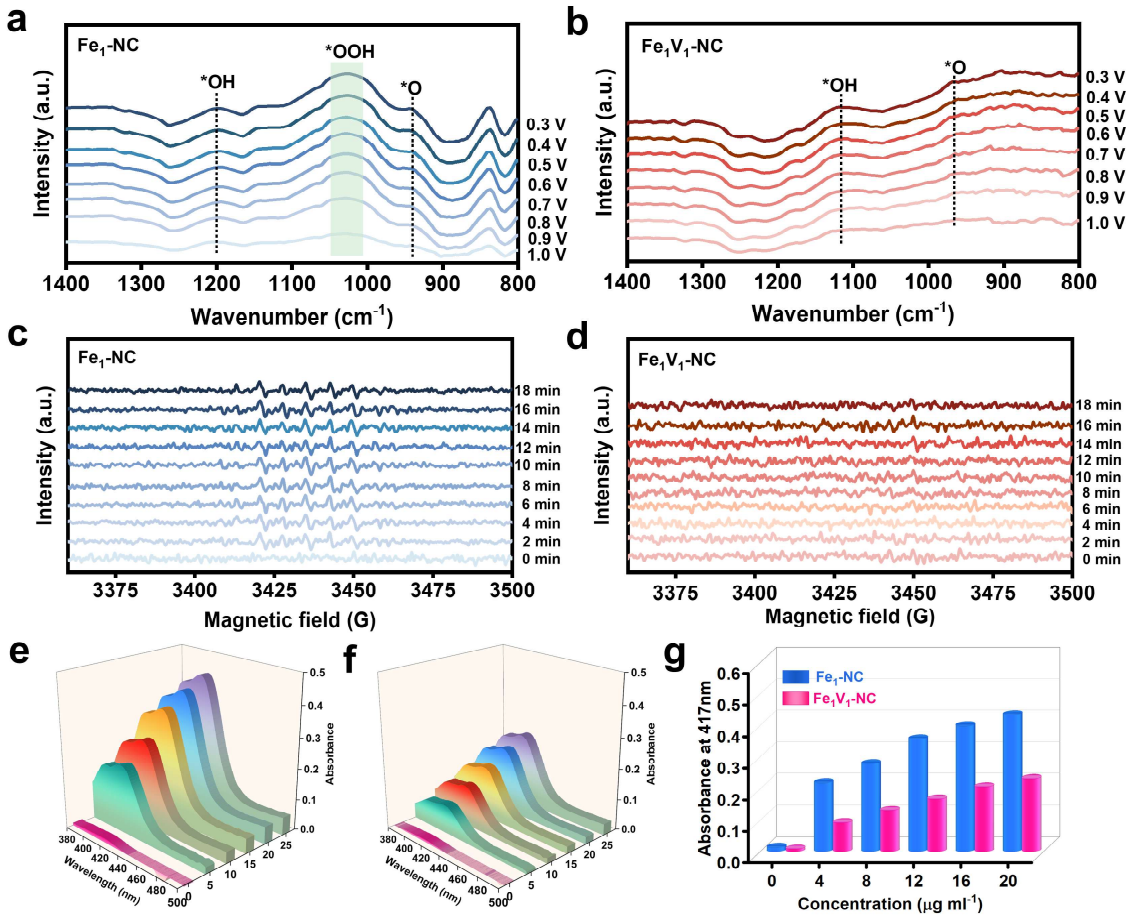

Figure 6. In situ ATR-SEIRAS spectroscopies of (a) Fe_1-NC and (b) Fe_1V_1-NC, respectively. In situ EPR spectra for monitoring ·OH radical of (c) Fe_1-NC and (d) Fe_1V_1-NC, respectively. UV-vis spectra of (e) Fe_1-NC and (f) Fe_1V_1-NC obtained by ABTS radical test. (g) Comparison of the absorbance at 417 nm for Fe_1-NC and Fe_1V_1-NC

We further performed *in situ* electron paramagnetic resonance (EPR) spectroscopy to detect characteristic signals of the intermediates to corroborate the ATR-SEIRAS analysis above. 5,5-dimethyl-1-pyrroline N-oxide (DMPO) is used to capture the active species, for which an aliquot is then transferred from the quartz reactor cell to the EPR sample chamber during the corresponding ORR.[51] As shown in Figures 6c and 6d, Fe_1-NC exhibits significantly higher ·OH signals in the range of 3415 – 3455 Gauss, whereas these characteristic peaks are barely visible in the spectra for Fe_1V_1-NC, hence corroborating the unique pathway on Fe_1V_1-NC with no radical generation. Interestingly, the characteristic peaks of ·OH remain undiminished after 18 min for Fe_1-NC, indicative of a slow conversion of the ·OH radicals with a longer lifetime. We also design radical trapping experiments to monitor the ROS formation during ORR. We chose 2,2-azinobis-(3-rthylbenzoline-6-sulfonate) (ABTS) to trap ROS. ABTS is easily oxidized by ROS to form ox-ABTS and the color of the system changes from colorless to green. This can be quantified by monitoring the absorbance changes at 417 nm. The measurement is initiated by the addition of a controlled amount of H_2O_2 to the reaction system. In Figure 6e-6g, the absorbance for Fe_1V_1-NC is notably lower at each concentration point when compared to that of Fe_1-NC, confirming again that Fe_1V_1-NC generates fewer ROS radicals during ORR. These investigations collectively demonstrate that, unlike Fe_1-NC, Fe_1V_1-NC follows a rather unique pathway that effectively reduces the generation of ROS radicals, which suppresses the associated catalyst corrosions and promotes robust long-term ORR activity.

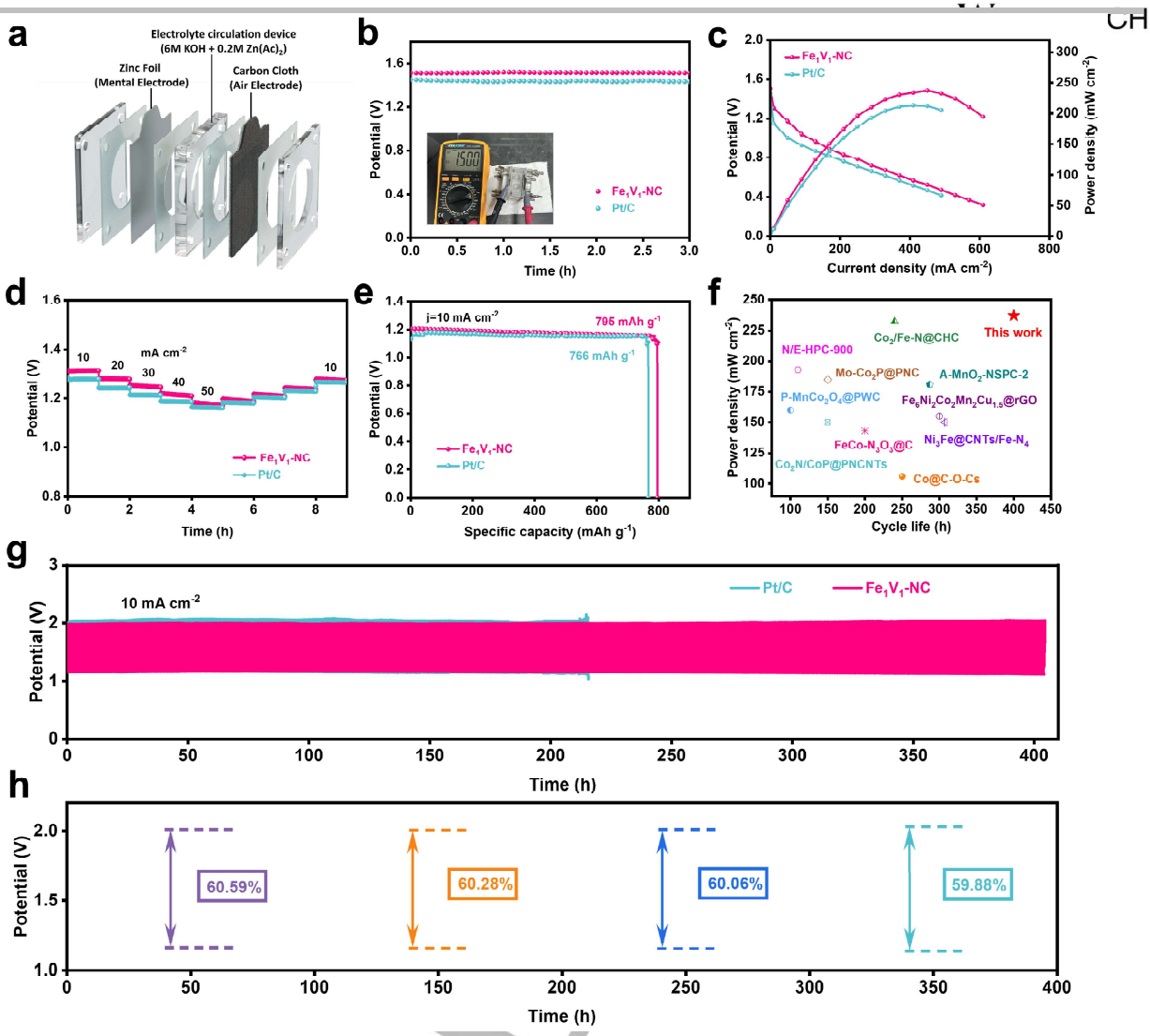

Figure 7. (a) Configuration diagram of the ZABs. (b) Open-circuit potential (OCP) curves (the inset is the picture of Fe_1V_1-NC-based ZAB connected to a multimeter). (c) Discharge polarization curves and corresponding power density curves of Fe_1V_1-NC and Pt/C. (d) Galvanostatic discharge curves of Fe_1V_1-NC-based and Pt/C-based ZABs at various current densities from 10 to 50 mA·cm^{-2}. (e) Galvanostatic discharge curves (Zn-mass-normalized specific capacities) of Fe_1V_1-NC and Pt/C at 10 mA·cm^{-2}. (f) Comparison of Zn-air batteries performance with that of the PGM-free electrocatalysts reported previously. These data are also summarized in Table S8 with references. (g) Galvanostatic discharge/charge cycling performance of Fe_1V_1-NC-based and Pt/C-based ZABs at 10 mA·cm^{-2}, and (h) corresponding discharge voltage stability.

Zn-Air Batteries Performance

To evaluate the performance of the catalysts at the device level, we assembled a rechargeable zinc-air battery (ZAB) using Fe_1V_1-NC as the cathode catalyst and a zinc plate as the anode in an electrolyte solution containing 6 M KOH and 0.2 M $Zn(Ac)_2$ (Figure 7a and S36). For comparison, the ZAB performances of Pt/C (20 wt.%) and Fe_1-NC have also been measured. The Fe_1V_1-NC-based ZAB registers a slightly higher open-circuit potential (OCP, up to 1.50 V) than the commercial Pt/C-based (1.47 V) and Fe_1-NC-based (1.38 V) ZABs as shown in Figure 7b and S37a respectively, indicative of a lower overpotential of Fe_1V_1-NC than that of commercial Pt/C and Fe_1-NC. The discharge polarization and corresponding power density curves are shown in Figure 7c and S37b, where the Fe_1V_1-NC-based ZAB presents a higher peak power density (237 mW·cm^{-2}) than the Pt/C-based (211 mW·cm^{-2}) and Fe_1-NC-based (125 mW·cm^{-2}) ZABs. The galvanostatic discharge curves in Figure 7d and S37c depict the similar trend where the operating potential of the Fe_1V_1-NC-based ZAB outperforms that of the Pt/C-based and Fe_1-NC-based ZABs across the range of discharge current densities from 10 to 50 mA·cm^{-2}. The batteries' operating potentials, except for Fe1-NC-based ZAB, show a quick and reasonable recovery with returning the current density from 50 to 10 mA·cm^{-2}. The specific capacity (795 mAh·g^{-1}, normalized to the mass of zinc) of the Fe_1V_1-NC-based ZAB at j = 10 mA·cm^{-2} also surpasses that of the Pt/C-based (766 mAh·g^{-1}) and Fe_1-NC-based (723 mAh·g^{-1}) ZABs as shown in Figure 7e and S37d. The cycling performances of both ZABs are evaluated via galvanostatic discharge-charge cycling tests. The cycling

stability of the Fe_1V_1-NC-based ZAB for both the discharge and charging processes at 10 mA·cm^{-2} exceeds 400 h (600 cycles) without notable discharge voltage changes, showing its impressive cycling durability (Figure 7g). In contrast, both Pt/C-based and Fe_1-NC-based ZABs exhibit losses in the energy efficiency up to 200 h and 95 h, respectively. Importantly, the Fe and V dissolution levels are as low as to 0.30% and 0.37% after the initial 40 h (Table S9), evidencing the high structural robustness of Fe_1V_1-NC. These contrasted ZAB performances of Fe_1V_1-NC and Fe_1-NC further support the dissociative mechanism promoted by Fe_1V_1-NC with limited ROS-related degradation and enhanced catalytic performance. Figure 7h shows the voltage efficiency of the Fe_1V_1-NC-based ZAB stays at ~60% with negligible changes (less than 1%) throughout the 400 hours of discharge and charge cycles. The performance of the Fe_1V_1-NC-based ZAB presented here is leading amongst the ZABs that employ PGM-free catalysts in the latest reports in the literature as summarized in Figure 7f and Table S8. Particularly, the exceptional cycling durability achieved by the Fe_1V_1-NC-based ZAB is a strong testimony to the strategy of circumventing ROS generation to improve the stability of catalysts during an ORR by introducing Fe-V atomic pair in Fe_1V_1-NC. Finally, we conducted tests for Fe_1V_1-NC and Fe_1-NC as catalysts in anion exchange membrane fuel cells (AEMFCs). Fe_1V_1-NC outperformed Fe_1-NC in terms of the highest current density and peak power density under all three conditions tested (Figure S38). The preliminary durability tests in AEMFCs confirms the superior stability of Fe_1V_1-NC over Fe_1-NC as shown in Figure S39. These results corroborate the other electrochemical measurements.

Conclusion

In summary, we demonstrated an effective strategy to switch the mechanistic ORR pathway and, therefore, improve the intrinsic ORR stability via designing catalysts guided by DFT calculations. The as-prepared Fe_1V_1-NC with Fe-V atomic pairs exhibit a unique active site configuration (N_2Fe-N_2-VN_2), allowing an O=O bond direct-cleavage pathway. This unique ORR pathway not only generates a lower reaction barrier that enhances its ORR activity, but also circumvents the ROS radical generations, which significantly improve the stability of the catalyst. Fe_1V_1-NC achieved an outstanding ORR activity with E_{onset} and $E_{1/2}$ at 1.02 and 0.89 V vs. RHE, respectively. The remarkable ORR stability of Fe_1V_1-NC is characterized by losses in $E_{1/2}$ at the low rate of 3.2×10^{-4} mV per cycle over 50,000 CV cycles. In situ characterizations and analyses revealed that the transformation of ORR pathway between Fe_1V_1-NC and Fe_1-NC led to distinct differences in ROS radical generation, fundamentally enhancing ORR stability of Fe_1V_1-NC. The Fe_1V_1-NC-based ZAB exhibited excellent cycling durability with no detectable voltage decay over 400 h charge-discharge operation, outperforming most of the PGM-free catalysts reported lately. These findings elucidate the effect of different ORR pathways on the catalytic stability of ORR catalysts, providing fresh insights for developing stable and efficient catalytic systems towards sustainable energy conversion technologies.

Acknowledgements

This study was financially supported by Natural Science Foundation of China (Grant No. 22308387, 22238013, 22002189 and U1932148), Guangdong Basic and Applied Basic Research Foundation (Nos. 2023A1515011935), Shanghai Advanced Research Institute (Grant No. E55G211ZZ1); Chinese Academy of Sciences (Grant No. E52G431401), Fundamental Research Funds for the Central Universities of Central South University. WT and PF acknowledge the support from ENEPORT project (EAPA_0016/2022) funded by Interreg Atlantic Area and the European Union. We acknowledge the technical support from Advanced Photon Source (APS) of Argonne National Laboratory (ANL). XAS measurements were performed at 12-BM beamline. The use of APS with the beam time award (https://doi.org/10.46936/APS-188704/60013232) is supported by Department of Energy under DE-AC02-06CH11357.

Keywords: Oxygen reduction reaction • Fe-N-C • ROS generation • Stability • Zn-air battery

[1] S. Liu, C. Li, M. J. Zachman, Y. Zeng, H. Yu, B. Li, M. Wang, J. Braaten, J. Liu, H. M. Meyer, M. Lucero, A. J. Kropf, E. E. Alp, Q. Gong, Q. Shi, Z. Feng, H. Xu, G. Wang, D. J. Myers, J. Xie, D. A. Cullen, S. Litster, G. Wu, *Nat Energy* **2022**, *7*, 652-663.
[2] T. Sun, Y. Li, T. Cui, L. Xu, Y.-G. Wang, W. Chen, P. Zhang, T. Zheng, X. Fu, S. Zhang, Z. Zhang, D. Wang, Y. Li, *Nano Lett.* **2020**, *20*, 6206-6214.
[3] Y. Cao, Y. Liu, X. Zheng, J. Yang, H. Wang, J. Zhang, X. Han, Y. Deng, G. Rupprechter, W. Hu, *Angew. Chem. Int. Ed.* **2025**, *64*, e202423556.
[4] B. Tang, Q. Ji, X. Zhang, R. Shi, J. Ma, Z. Zhuang, M. Sun, H. Wang, R. Liu, H. Liu, C. Wang, Z. Guo, L. Lu, P. Jiang, D. Wang, W. Yan, *Angew. Chem. Int. Ed.* **2025**, *64*, e202424135.
[5] P. Wu, L.-L. Shen, W. Zhao, H. Yu, J. Wang, Y. Xu, X. Li, Y. Wang, G.-R. Zhang, D. Mei, *Appl. Catal., B* **2025**, *375*, 125408.
[6] H. Tian, A. Song, P. Zhang, K. Sun, J. Wang, B. Sun, Q. Fan, G. Shao, C. Chen, H. Liu, Y. Li, G. Wang, *Adv. Mater.* **2023**, *35*, 2210714.
[7] R. Sui, B. Liu, C. Chen, X. Tan, C. He, D. Xin, B. Chen, Z. Xu, J. Li, W. Chen, Z. Zhuang, Z. Wang, C. Chen, *J. Am. Chem. Soc.* **2024**, *146*, 26442-26453.
[8] L. Jiao, T. A. Arman, S. Hwang, J. Fonseca, N. Okolie, E. Shaaban, G. Li, E. Liu, U. Pasaogullari, S. K. Babu, S. Mukerjee, J. S. Spendelow, D. A. Cullen, F. Jaouen, Q. Jia, *Adv. Energy Mater.* **2024**, *14*, 2303952.
[9] S. Zhang, J. Yang, L. Yang, T. Yang, Y. Liu, L. Zhou, Z. Xu, X. Zhou, J. Tang, *Appl. Catal., B* **2024**, *359*, 124485.
[10] X. Li, G. Ye, W. Zhu, M. Tian, R. Wang, S. Liu, Z. He, *ACS Nano.* **2024**, *18*, 24505-24514.
[11] Y. Jiang, Z. Yu, X. Zhou, X. Cheng, H. Huang, F. Liu, Y. Yang, S. He, H. Pan, H. Yang, Y. Yao, X. Rui, Y. Yu, *Adv. Mater.* **2022**, *35*, 2208873.
[12] L. Huang, H. Niu, C. Xia, F. M. Li, Z. Shahid, B. Y. Xia, *Adv. Mater.* **2024**, *36*, 2404773.
[13] H. Zhang, H. C. Chen, S. Feizpoor, L. Li, X. Zhang, X. Xu, Z. Zhuang, Z. Li, W. Hu, R. Snyders, D. Wang, C. Wang, *Adv. Mater.* **2024**, *36*, 2400523.
[14] L. Lyu, X. Hu, S. Lee, W. Fan, G. Kim, J. Zhang, Z. Zhou, Y.-M. Kang, *J. Am. Chem. Soc.* **2024**, *146*, 4803-4813.
[15] B. Wang, X. Yang, Y. Fang, X. Zhou, R. Jiang, X. Han, S. Wang, Y. Lin, J. Liu, X. Duan, *Adv. Funct. Mater.* **2024**, *34*, 2404828.
[16] D. Xia, X. Tang, S. Dai, R. Ge, A. Rykov, J. Wang, T. H. Huang, K. W. Wang, Y. Wei, K. Zhang, J. Li, L. Gan, F. Kang, *Adv. Mater.* **2022**, *35*, 2204474.
[17] C. B. Musgrave, J. Su, P. Xiong, Y. Song, L. Huang, Y. Liu, G. Li, Q. Zhang, Y. Xin, M. M.-J. Li, R. T. K. Kwok, J. W. Y. Lam, B. Z. Tang, W. A. Goddard, R. Ye, *J. Am. Chem. Soc.* **2025**, *147*, 3786-3795.
[18] J. Liu, Y. Liu, B. Nan, D. Wang, C. Allen, Z. Gong, G. He, K. Fu, G. Ye, H. Fei, *Angew. Chem. Int. Ed.* **2025**, *64*, e202425196.
[19] Y. Zhao, P. Yin, Y. Yang, R. Wang, C. Gong, J. Li, J. Guo, Q. Wang, T. Ling, *Angew. Chem. Int. Ed.* **2025**, *64*, e202419501.
[20] F. Liu, D. Zhang, F. She, Z. Yu, L. Lai, H. Li, L. Wei, Y. Chen, *ACS Catal.* **2024**, *14*, 9176-9187.
[21] Qingtao Liu, Weihao Liu, Xin Wan, Weiwei Chen, Xiaozhi Liu, Xiaofang Liu, Jiaxiang Shang, Jungang Miao, Dong Su, Xin Sun, J. Shui*, *Adv. Funct. Mater.* **2025**, 2507376.
[22] H. Jiang, J. He, S. Zhou, M. Yuan, L. Lin, Z. Sun, G. Sun, *ACS Nano.* **2025**, *19*, 12161-12169.
[23] K. Ding, J. Hu, W. Jin, L. Zhao, Y. Liu, Z. Wu, B. Weng, H. Hou, X. Ji, *Adv. Funct. Mater.* **2022**, *32*, 2201944.
[24] F. Xia, B. Li, B. An, M. J. Zachman, X. Xie, Y. Liu, S. Xu, S. Saha, Q. Wu, S. Gao, I. B. Abdul Razak, D. E. Brown, V. Ramani, R. Wang, T. J. Marks, Y. Shao, Y. Cheng, *J. Am. Chem. Soc.* **2024**, *146*, 33569-33578.
[25] N. Xue, X. Xue, A. Aihemaiti, H. Zhu, J. Yin, *Small* **2024**, *20*, 2311034.
[26] Y. Zhao, Z. Gao, S. Zhang, X. Guan, W. Xu, Y. Liang, H. Jiang, Z. Li, S. Wu, Z. Cui, S. Zhu, *Adv. Funct. Mater.* **2025**, 2504260.
[27] X. Y. Cheng, X. T. Jiang, S. H. Yin, L. F. Ji, Y. N. Yan, G. Li, R. Huang, C. T. Wang, H. G. Liao, Y. X. Jiang, S. G. Sun, *Angew. Chem. Int. Ed.* **2023**, *62*, e202306166.
[28] Z. Sun, Y. Zhong, H. Sui, J. Liu, P. Xie, S. Ding, Y. Su, *Adv. Funct. Mater.* **2024**, *34*, 2410774.

[29] H. Niu, L. Huang, Y. Qin, R. Qi, B. Mei, D. Wu, F.-M. Li, B. You, Q. Li, Y. Yao, Z. Wang, T. Yao, S. Ding, W. Guo, Y. Chen, Y. Su, F. Song, B. Y. Xia, *J. Am. Chem. Soc.* **2024**, *146*, 22650-22660.
[30] H. Xie, X. Xie, G. Hu, V. Prabhakaran, S. Saha, L. Gonzalez-Lopez, A. H. Phakatkar, M. Hong, M. Wu, R. Shahbazian-Yassar, V. Ramani, M. I. Al-Sheikhly, D.-e. Jiang, Y. Shao, L. Hu, *Nat. Energy* **2022**, *7*, 281-289.
[31] L. Ran, Y. Xu, X. Zhu, S. Chen, X. Qiu, *ACS Nano.* **2023**, *18*, 750-760.
[32] Z. Wang, Z. Lu, Q. Ye, Z. Yang, R. Xu, K. Kong, Y. Zhang, T. Yan, Y. Liu, Z. Pan, Y. Huang, X. Lu, *Adv. Funct. Mater.* **2024**, *34*, 2315150.
[33] D. Xue, Y. Yuan, Y. Yu, S. Xu, Y. Wei, J. Zhang, H. Guo, M. Shao, J.-N. Zhang, *Nat. Commun.* **2024**, *15*, 5990.
[34] X. Zhao, H. Cheng, X. Chen, Q. Zhang, C. Li, J. Xie, N. Marinkovic, L. Ma, J.-C. Zheng, K. Sasaki, *J. Am. Chem. Soc.* **2024**, *146*, 3010-3022.
[35] X. Shen, T. Nagai, F. Yang, L. Q. Zhou, Y. Pan, L. Yao, D. Wu, Y.-S. Liu, J. Feng, J. Guo, H. Jia, Z. Peng, *J. Am. Chem. Soc.* **2019**, *141*, 9463-9467.
[36] X. Wan, Q. Liu, J. Liu, S. Liu, X. Liu, L. Zheng, J. Shang, R. Yu, J. Shui, *Nat. Commun.* **2022**, *13*, 2963.
[37] Z. Huang, M. Li, X. Yang, T. Zhang, X. Wang, W. Song, J. Zhang, H. Wang, Y. Chen, J. Ding, W. Hu, *J. Am. Chem. Soc.* **2024**, *146*, 24842-24854.
[38] A. Han, W. Sun, X. Wan, D. Cai, X. Wang, F. Li, J. Shui, D. Wang, *Angew. Chem. Int. Ed.* **2023**, *62*, e202303185.
[39] H. Sui, Q. Guo, M. Xiang, X. Kong, J. Zhang, S. Ding, Y. Su, *J. Phys. Chem. Lett.* **2024**, *15*, 8257-8264
[40] X. X. Li, Y. Yan, X. N. Zheng, Y. Yao, Y. Liu, *Chem. Eng. J.* **2022**, *444*, 136363.
[41] R. Li, W. Fan, P. Rao, J. Luo, J. Li, P. Deng, D. Wu, W. Huang, C. Jia, Z. Liu, Z. Miao, X. Tian, *ACS Nano.* **2023**, *17*, 18128-18138.
[42] Y. Jiang, Z. Yu, X. Zhou, X. Cheng, H. Huang, F. Wu, L. Yang, S. Wu, H. Pan, H. Yang, Y. Yao, X. Rui, Y. Yu, *Adv. Mater.* **2022**, *35*, 2208873.
[43] S. Pérez-Rodríguez, D. Torres, M. T. Izquierdo, A. Zitolo, N. Bibent, M. Sougrati, F. Jaouen, A. Celzard, V. Fierro, *Small* **2024**, *21*, 2406887.
[44] A. Dessalle, J. Quílez-Bermejo, J. W. Hounfodji, M. Badawi, A. Zitolo, M. Emo, M. T. Izquierdo, F. Xu, V. Fierro, A. Celzard, *Small* **2025**, *21*, 2409474.
[45] D. Zhang, F. She, J. Chen, L. Wei, H. Li, *J. Am. Chem. Soc.* **2025**, *147*, 6076-6086.
[46] Y. C. Yao, T. Jiang, S. Y. Lim, C. Frandsen, Z. J. Li, Y. B. Dou, F. Y. Wu, J. B. Qin, J. Z. Zou, E. Stamate, W. J. Zhang, *Small* **2023**, *19*, 2304655.
[47] Z. Sun, Y. Zhong, H. Sui, J. Liu, P. Xie, S. Ding, Y. Su, *Adv. Funct. Mater.* **2024**, *34*, 2410774
[48] C. L. Liu, R. Z. Yang, J. C. Wang, B. W. Liu, X. W. Chang, P. X. Feng, X. Z. Zhang, L. J. Zhong, X. L. Zhao, L. Niu, S. Y. Gan, Y. B. Xi, M. Huang, H. Wang, *Angew. Chem. Int. Ed.* **2025**, e202501266.
[49] X. Jia, Q. Meng, R. Zheng, X. Liu, Y. Zhao, C. Liu, M. Xiao, W. Xing, *Renewables* **2023**, *1*, 694-719.
[50] L. Meng, S. Niu, Z. Wei, X. Qin, F. Naseem, W. Wei, *Appl. Catal., B* **2025**, *367*, 125080.
[51] J. He, Z. Li, P. Feng, G. Lu, T. Ding, L. Chen, X. Duan, M. Zhu, *Angew. Chem. Int. Ed.* **2024**, *63*, e202410381.

Table of Contents

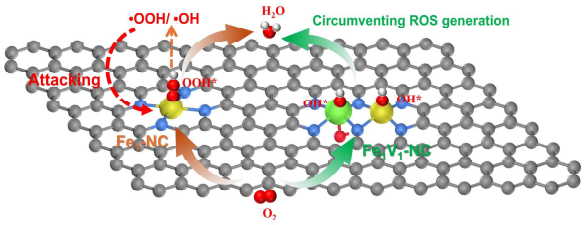

The designed Fe-V atomic pair catalyst (Fe_1V_1-NC) proceeds via direct O=O breaking pathway and thus circumvents the ROS radical generations, fundamentally enhancing ORR stability for perdurable zinc-air batteries.

Lan Ran, Yichen Zhang, Wenming Tong, Long Chen, Maoyu Wang, Hua Zhou, Pau Farràs, Shanyong Chen*, Xiaoqing Qiu**

Circumventing Radical Generation on Fe-V Atomic Pair Catalyst for Robust Oxygen Reduction and Zinc-Air Batteries